The International Journal of Advanced Manufacturing Technology (2023) 126:273–289
https://doi.org/10.1007/s00170-023-11105-w

ORIGINAL ARTICLE

Combined effect of the interlayer temperature with travel speed on features of thin wall WAAM under two cooling approaches

Felipe Ribeiro Teixeira[1] · Fernando Matos Scotti[1] · Vinicius Lemes Jorge[1] · Américo Scotti[1,2]

Received: 18 November 2022 / Accepted: 12 February 2023 / Published online: 24 February 2023

Abstract

This work presents the evaluation of the interlayer temperature (IT) with travel speed (TS) combined effect for a given wire feed speed (WFS) on operational, geometrical, and metallurgical features of thin walls with the same width deposited by wire arc additive manufacturing (WAAM) with a low alloy steel, using or not active cooling. A preliminary experimental design was carried out to define a range of IT that could prevent the molten pool from running down and, then, be used in the main experimental design. The main tests were planned and performed to find different IT and TS combinations for a given WFS capable of depositing walls with the same target effective wall width. After selecting the parameters, six walls were deposited, three under natural cooling (NC) and three under near immersion active cooling (NIAC). A more significant temperature variability along the layer length (ΔT/ΔLL) is observed in increasing IT-TS combination and under NIAC. Regardless of the cooling approach, a worse surface aspect was observed with lower IT and TS. However, NC or NIAC do not affect the wall width (effective or external) or the layer height. On the other hand, they are affected by the IT with TS combination. A shorter production time was obtained on the walls with NIAC and higher IT-TS. No marked microstructural differences were observed comparing the walls, regardless of the cooling approach. However, microstructure tempering (hardness reduction) was observed in the walls deposited with NC using higher IT levels.

Keywords WAAM · Idle time · Production · Geometrical features and surface finishing

1 Introduction

The interlayer temperature (IT) is one of several variables in the wire arc additive manufacturing (WAAM) processes. There are other important variables, such as the deposition material [1], the wire feed speed, and the travel speed [2]. The importance of monitoring IT comes from the interest in ensuring the repeatability of deposition between layers. As mentioned by different authors [3, 4], working with a constant interlayer temperature is recommended to keep the homogeneity of material properties. So, monitoring this parameter is also essential to understand possible metallurgical transformations that a given material may undergo during deposition and, consequently, predicting the mechanical properties of the deposited component. However, Da Silva et al. [5] mention that the term "interlayer temperature" in additive manufacturing is still not very clear. In fact, it is common to have the interlayer temperature in additive manufacturing referred to as interpass temperature, as has been done by several authors [6–12]. Also, still according to Da Silva et al. [5], this designation is used due to the similarity with the concept adopted in welding procedures, which considers a temperature range that the joint needs to be before the deposition of a new pass. Therefore, since in additive manufacturing layers upon layers are deposited until the final build of the component, the terminology "interlayer temperature" seems to be more appropriate, as also discussed by Jorge et al. [13].

✉ Américo Scotti
americo.scotti@hv.se; ascotti@ufu.br

Felipe Ribeiro Teixeira
teixeira.304@hotmail.com

Fernando Matos Scotti
fernandomscotti@gmail.com

Vinicius Lemes Jorge
viniciuslemesj@hotmail.com

[1] Center for Research and Development of Welding Processes, Federal University of Uberlandia, Uberlândia, MG 38400-652, Brazil

[2] Department of Engineering Science, University West, Trollhättan SE 461 86, Sweden

Depending on the level of variation and the material evaluated, interlayer temperature can influence the formation of defects or non-conformities, the geometry, microstructure, and mechanical properties of components deposited by WAAM. By evaluating the effect of heat accumulation on a Ti6Al4V wall, Wu et al. [14] found greater oxidation on the layer surface when the interlayer temperature was increased from 150 to 300 °C, approximately. Regarding the possibility of non-conformities formation, Derekar et al. [7] found a greater amount of pores in a wall of Al–Mg (AWS ER5356) deposited with a TI of 50 °C than with 100 °C. According to the authors, the condition of lower interlayer temperature (more refined microstructure) presented more available grain boundaries, which served as sites for hydrogen trapping and resulted in porosities. In terms of the geometric point of view, Wang et al. [15] showed that as the interlayer temperature increases, the width and height of the layer tend to enlarge and shorten, respectively. Furthermore, both Geng et al. [10] (using an aluminium alloy) and Knezovic et al. [16] (using duplex stainless steel) showed better surface finishing when higher levels of interlayer temperature were used, facilitating a possible machining step after deposition. However, this behaviour may not be the same for all materials, since Spencer et al. [17] showed the opposite effect when a C-Mn steel was used as the feedstock.

Still in this context, Ali et al. [18] evaluated the influence of interlayer temperature on the microstructure of walls deposited with a hot-work tool steel, where two regions (tempered and non-tempered) were identified along the build direction. According to the authors, as long as the IT is above the starting temperature of martensite formation, the microstructure remains in the austenitic field. With this, a more homogeneous microstructure compatible with the characteristics of the non-tempered region is obtained. In another work, regarding the deposition of high-strength steel, Müller et al. [12] found martensite formation with a higher interlayer temperature level. Consequently, higher tensile strength and lower yield and impact strength were observed. Some authors did not provide evidence of any marked microstructural change when the interlayer temperature was altered. These are the cases of Shen et al. [9], who evaluated interlayer temperature levels between 280 and 400 °C in walls deposited with a Fe_3Al-based iron aluminide, and Chen et al. [6], who used IT between 100 and 400 °C in components of a nickel-aluminium bronze (NAB) alloy.

Looking from an operational perspective, natural cooling of a given component can be a good option when high levels of interlayer temperature need to be maintained, as the waiting times between one layer and another (idle times) are usually not significant in this case. The control of the microstructure through IT is another possibility. However, the idle times may vary according to the conditions that control the heat transfer of the component, such as the arc energy, part dimensions (width and height), and physicochemical properties of the deposited material. Although there exist conditions that favour heat exchange (low arc energy, wide wall, and high material thermal conductivity), the idle time can be considerably increased when lower interlayer temperature (closer to room temperature) must be reached. To mitigate heat accumulation and, at the same time, this production problem, approaches involving forced cooling directly on the component (active cooling) or on the substrate (passive cooling) are often used to control IT during deposition. Although approaches with passive cooling are more accessible and widely reported in the literature [18–20], they take longer to cool down to a given interlayer temperature than those using active cooling. In addition, its efficiency tends to be considerably reduced as the distance from the substrate increases. Among the active cooling approaches are those that use air to promote forced convection. In these cases, the jet can be blown either by the torch nozzle itself during the idle time between layers [20] or by an additional nozzle focused directly on the component [21]. There are also cases where forced convection was promoted by trailing [22, 23]. Ma et al. [22], for example, evaluated cooling with three different gases (air, CO_2, and N_2) using a shielding cover positioned behind the torch to promote cooling during deposition. According to the authors, CO_2 resulted in more efficient cooling. Work involving near immersion active cooling (NIAC) in a water bath has also been proposed [19, 24, 25]. In this approach, the deposition is carried out inside a tank, where controlled filling water is used to cool the component during the deposition.

Given the above (breadth of research focuses and disagreement of results), it is clear the importance of better understanding how the interlayer temperature can influence different operational aspects of WAAM and the role of the cooling approaches to reduce the idle time between layers. However, it should be kept in mind that other variables, such as wire feed speed (WFS) and travel speed (TS), also control idle time, as they influence the arc energy (as can be seen in Ali et al. [18] and Rodrigues et al. [26]). Thus, as important as understanding the effects of different levels of IT, WFS, and TS, it is to know how to use them combined to achieve a target geometrical feature. For example, it is hypothetically possible to obtain the same wall width with different combinations of WFS with TS (arc power levels), as long as suitable IT is selected. As this gap has been unexplored by the literature until now, it becomes relevant to study it. Thus, the global objective of this work is to evaluate the combined effect of the interlayer temperature with travel speed for a given wire feed speed on the operational (surface finishing, production time and temperature profile), geometrical (wall width and height), and

metallurgical (microstructure and microhardness) features of thin walls with the same width deposited by WAAM, using or not active cooling.

2 Methodology and experimental procedure

Defining beforehand some concepts and terminologies is necessary to understand this work better. First, the application of this research is restricted to WAAM of high-strength low-alloy steel thin walls (one pass per layer and with no torch oscillation in the transverse direction). By definition, the wall width can be asserted as effective or external. Regardless of other concepts of effective width/thickness used in the literature [27], a similar meaning to that used by Martina et al. [28] is admitted in this work, that is, the effective wall width represents that obtained if the lateral undulations of the walls, intrinsic to the WAAM, are removed (the nominal design width). On the other hand, the external wall width is measured over the undulation peaks on the sides of the wall. As reaching a given effective wall width is what matters from a designing point of view, a given effective wall width was arbitrarily chosen for this study. It was used as the fixed comparison parameter for the different combinations of the interlayer temperature (IT) and travel speed (TS) for a given wire feed speed (WFS). The concept of interlayer temperature in this current work is, in turn, defined as the temperature value taken as a reference to start the deposition of a new layer, considering a particular measurement point located on the printable part. In the present case, this temperature is measured by an infrared pyrometer positioned at the same distance in front of the heat source (the arc). In other words, only after this temperature has been reached between layers, the deposition of a new layer begins.

In this scope, preliminary tests were carried out to define an interlayer temperature range to be used in the experimental design, capable of preventing the molten pool from running down. For this, two combinations of WFS with TS were chosen from a working envelope published by Teixeira et al. [29] for thin walls WAAM manufactured. This working envelope was made for a wire with a chemical composition compatible with the one used in this work (principle of parameter transportability). To define a wide enough interlayer temperature range, but capable of preventing unstable molten pool, the most critical conditions of the working envelope were chosen (larger pool volume is more critical in running towards the sides). Following this, the two chosen combinations (WFS at 5 m/min-TS at 21.7 cm/min and WFS at 3 m/min-TS at 15 cm/min) are the operational extremes of the mentioned envelope. Five levels of interlayer temperature (100, 200, 300, 400, and 500 °C) were proposed for each WFS with TS combination, totalising 10 different walls to be built (Table 1). A minimum height of 40 mm was a target for each wall. No forced cooling was used at this step of the work. The effect of interlayer temperature was assessed based on the surface appearance, production time, temperature profile, and wall geometry. As will be discussed in Section 3.1, the wide range of interlayer temperatures in Table 1 proved to be functional.

Table 1 Experimental matrix of preliminary tests

Run	WFS (m/min)	TS (cm/min)	IT (°C)
1	3	15.0	100
2	3	15.0	200
3	3	15.0	300
4	3	15.0	400
5	3	15.0	500
6	5	21.7	100
7	5	21.7	200
8	5	21.7	300
9	5	21.7	400
10	5	21.7	500

Once this range was defined, the main experimental design (main tests) was planned and executed, aiming at finding different IT-TS combinations for a given WFS capable of depositing three walls with the same target effective wall width (WW_{eff}). A WW_{eff} of 5.7 mm was arbitrarily chosen. The geometrical features of the preliminary tests were used as a starting point to find the parameter combinations to fill the design of experiments (DoE). Some tests were realised to confirm and adjust the parameters to the desired WW_{eff}. Since each combination of process parameters can result in a different layer height, the number of layers changed for each wall, and it has been established to have a minimum height of 40 mm. A bidirectional layer deposition strategy was used for all walls, that is, the deposition of a subsequent layer occurs in the opposite direction of the previous one. The three first walls were deposited without using active (forced) cooling between layers, that is, only natural cooling took place until the desired interlayer temperature was reached. However, to extend the reach of results and reduce idle time, three new walls were deposited using the same DoE, but now using the near immersion active cooling (NIAC) approach. This technique was carried out inside a tank with water gradually added as the layers were deposited, aiming at maintaining the same distance between the water line and the last layer edge (parameter referred to as layer-edge to water distance, LEWD). The LEWD of 20 mm was set for all walls deposited with NIAC. To get that, water is pumped and circulated uninterruptedly inside the deposition tank. As the torch is raised, a magnetic floater activates a solenoid valve positioned at the water circuit inlet, allowing the water level to be established, consequently maintaining

the same LEWD throughout the wall building. More details about NIAC can be found in the literature [19, 24, 25].

An AWS ER90S-B3 wire (1.2-mm-diameter) was used as feedstock. This wire is basically a low carbon-low alloy (2.5Cr-1Mo) steel. The shielding gas was a mixture of 96%Ar + 4%CO_2, with a flow rate of 15 L/min. The cold metal transfer (CMT) version (synergistic line CMT 963) of the GMAW process was the deposition process. The contact tube-to-work distance (CTWD) was maintained at 16 mm during all depositions. Carbon steel plates (150 mm × 50 mm × 7.9 mm) were used as substrate. To keep the heat flow as constant as possible from the first layers, the substrates were positioned in a fixture with their narrow side facing up, mimicking a pre-wall. An A/D (analogue to digital conversion) board, operating for 8 s at an acquisition rate of 5 kHz and 14 bits (signal resolution), was employed to monitor the electrical signals (current and voltage) and wire feed speed. The mean and root mean square (RMS) of current and voltage, together with the average values of wire feed speed and arc energy per unit length, were determined for each layer. The arc energy per unit of length was determined using the instantaneous power (average of the products between point-to-point current and voltage) divided by the respective travel speed.

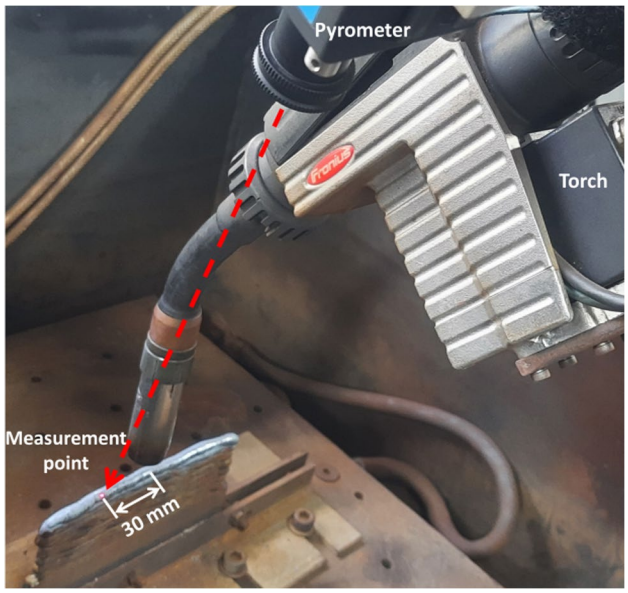

Fig. 1 Positioning of the temperature measurement point: in front of the molten pool, when the deposition direction (sense) was from right to left, and behind the pool, when the deposition direction was from left to right

2.1 Interlayer temperature measurement strategy

An infrared pyrometer (Mikron model MI-PE140) monitored the temperature profile over the deposited layers. The role of this temperature measurement was also to identify when the target interlayer temperature is reached. This pyrometer has a measurement range between 30 and 1000 °C, a resolution of 0.1 °C, and an acquisition rate of 10 Hz. The same procedure applied by Jorge et al. [13] was conducted to determine the emissivity to be regulated in the pyrometer software (a value of 0.99 was set for all depositions). It is important to clarify that the set emissivity is considered only as a correction parameter rather than its true value. This pyrometer was fixed to the torch axis and positioned (measurement point) at a distance of 30 mm from the wire centreline (Fig. 1). Since a bidirectional deposition strategy was used, only when the torch moved from right to left (based on Fig. 1), the pyrometer beam was ahead of the molten pool. In the opposite direction, monitoring was carried out behind the pool. Thus, when the layer deposition was ending, the pyrometer could be monitoring the temperature at the surface of the last layer deposited or at a point outside the wall. For the first situation, the temperature profile was monitored and a stopwatch was started to record and estimate the idle time to reach the target interlayer temperature for each wall. Once the target interlayer temperature was reached, the deposition of a new layer was started. For the second case, i.e., when the pyrometer was monitoring the temperature outside the wall, the idle time recorded for the previous layer was replicated.

To ensure the understanding of the temperature profiles, Fig. 2 shows a schematic of how the pyrometer displacement occurs during each cycle of torch movement (Fig. 2a) and its effect on the temperature profiles (Fig. 2b). The way in which the position of the measurement point affects the temperature profile was also detailed by Jorge et al. [13] and will only be briefly mentioned here. As can be seen, each frame in Fig. 2a has its timeline indicated by a red dashed line in Fig. 2b. Frame 1 of Fig. 2a represents the moment when the torch ended its trajectory from right to left — the torch is positioned at the left edge of the wall and the pyrometer beam is outside the wall, justifying the low temperature at that instant (line 1 of Fig. 2b). With the deposition resume (frame 2 of Fig. 2a), the torch moves to the right and the pyrometer starts recording the temperature behind the pool (line 2) until the layer deposition is completed (line 3). At the beginning (time before that marked by line 2), there is an abrupt increase in temperature coming from arc ignition that heats the material at the end and from the accumulated heat of the previous layer. As shown in Fig. 2b, it is precisely in the interval between lines 2 and 3 that the highest temperatures are recorded. With the layer finished (frame 3 of Fig. 2a), the arc is extinguished and the wall cools down again (between lines 3 and 4). When a target interlayer temperature is reached (indicated by line 4 and IT line crossing in Fig. 2b), a new layer begins to be deposited (frame 4 in Fig. 2a), but

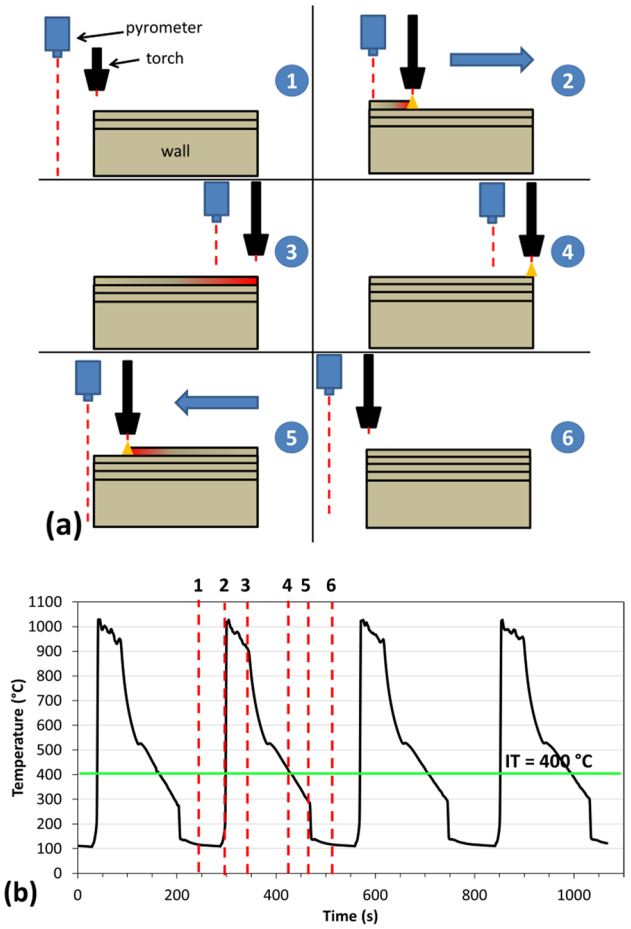

Fig. 2 **a** Frames illustrating the torch movement cycles and a schematic of the measurement point positioning in relation to the molten pool; **b** temperature trace resulting from the torch positioning (case of an IT of 400 °C), where the red dashed lines indicate the frames in a timeline

this time, the pyrometer starts measuring ahead of the molten pool. During this torch path, the temperature profile progressively reduces (from line 4 to line 5 of Fig. 2b) due to the presence of the thermal gradient. At a specific moment, the pyrometer starts to measure the temperature outside the wall again (frame 5 of Fig. 2a) and, consequently, the temperature drops abruptly to a plateau. The cycle is restarted at the time indicated by line 6 (frame 6 of Fig. 2a), which is equivalent to line 1.

2.2 Determination of the geometrical features

All built walls were scanned using a 3D scanner (HandySCAN 3D). Only the central region of the walls was evaluated to avoid the influence of non-conformities arising from the starting and ending deposition positions (Fig. 3a). The two sides of each wall were separated and exported as a set of data points (point cloud) to text files (.txt) using a dedicated computer programme (VXModel). Then, the point clouds corresponding to each side of the walls were read by a code (developed in Python language by Scotti [30]), which divided the meshes into sections with a spacing of 0.5 mm along the length of the wall. Since the reading file is a point cloud, it is required to establish a range in the axis along the length of the wall (Y) where the points will converge to a single profile. If the value of this parameter is too large, many points will converge to the same profile, making it difficult to quantify the geometry (saturated profile). On the other hand, if the value of this parameter is too small, the generated profile may have "holes". So, the smallest value capable of generating profiles without "holes" was selected (0.5 mm). Since the evaluated length was 90 mm, 180 sections were obtained altogether. For example, Fig. 3b shows a graph containing ten profiles obtained by the code for one side of the wall, where an axis perpendicular to the side of the wall (X), an axis along the length of the wall (Y), and an axis that coincides with the building direction (Z) are the reference axis.

To minimise the influence of possible outliers on the evaluated geometrical features, each section was divided into small sample lengths (λ_c) taken along the axis corresponding to the building direction (Z), as indicated in Fig. 3b. The value of λ_c is equal to the average layer height determined for each wall. Due to the existence of this parameter, maximum and minimum values of X and the difference between them were computed for each evaluated-in-a-section sample length. The developed code provides a file that contains an average of these values per section for each side of the walls. The averages of the maximum and minimum values of X

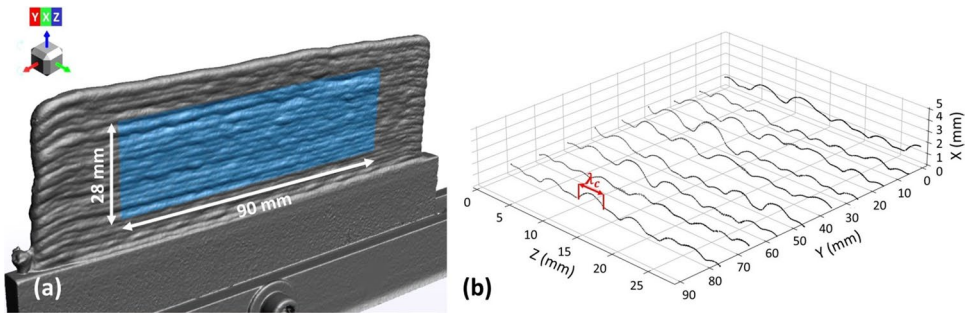

Fig. 3 **a** Region considered during the measurement of geometric features; **b** an example of the transversal profiles obtained by the code developed by Scotti [30]

from both sides of the wall are summed to determine the external wall width (WW_{ext}) and the effective wall width (WW_{eff}), respectively, considering the same section. The surface waviness (SW) of the wall, in turn, is quantified by the sum of the differences between the maximum and minimum values of X from both sides of the wall (considering the same section, of course) divided by two. Therefore, the measurement results of the geometrical features were determined by the mean and the standard deviation, considering the WW_{ext}, WW_{eff}, and SW values obtained from each of the 180 sections evaluated. An analogue calliper (0.05 mm resolution) was used to measure the total height of the wall at five different positions. These values were divided by the number of layers deposited, and then the average and its respective standard deviation were quantified to obtain the layer height (LH) result.

2.3 Metallurgical characterisation

Cross-sections were removed from each of the three walls with natural cooling and with near immersion active cooling. The samples were subjected to metallographic preparation and etched with 2% Nital for 20 s. Micrographs and microhardness measurements were taken at the top, centre, and bottom of the walls, discarding approximately 10 mm from the substrate to avoid a region that could be affected by dilution. A load of 100 g for 15 s was set for Vickers microhardness tests. For each region, the indentations were arranged in a vertical line with a spacing of 0.25 mm.

3 Results and discussions

3.1 Preliminary tests

Figure 4 shows the surface aspect of each deposited wall to confirm the maximum interlayer temperature (IT) suitability of the experimental matrix presented in Table 1. As seen, no interlayer temperature levels led to pool collapse. It is worth mentioning that IT was not increased further because the last layer turned partially incandescent (a condition reached when the temperature at the measurement point was above 550 °C, approximately) and it would imply a higher measurement error associated with the surface emissivity. It is important to add in this experimental description that about 15 layers were deposited to build each wall during the preliminary tests. As mentioned in Section 2, the layer deposition pattern was bidirectional (the odd layer always from left to right, with the pyrometer beam behind the arc, while the even layers were deposited on the reverse vectorial sense). For temperature monitoring, eight sequential layers were sampled from each wall, starting after 4 layers had been laid on the substrate (the first layer after the 4th was tagged as sampled 1st layer). Therefore, only the sampled 2nd, 4th, 6th, and 8th layers (with the pyrometer beam ahead of the arc) were useful in the temperature traces.

Figure 5 shows the temperature profiles as a function of the time after the eight sampled layers, considering the different interlayer temperature levels used with wire feed speed (WFS) at 3.0 m/min and travel speed (TS) at 15.0 cm/min in the DoE. Figure 6, in turn, presents analogous temperature profiles with a WFS at 5.0 m/min and TS at 21.7 cm/min. The times recorded for the deposition of eight layers (counting only when the pyrometer was detecting the layer) were summed with the idle times to cool down the layers, here referred to as dt_8. For a given travel speed (which defines the deposition time), the lower the interlayer temperature, the higher dt_8 (longer cooling times required). Comparing the two WFS and TS combinations at the same IT (Fig. 5 versus Fig. 6), the condition with WFS at 5.0 m/min and TS at 21.7 cm/min (Fig. 6) presented lower dt_8 due to the higher travel speed used (faster deposition time).

Even out of the scope, yet noteworthy, is the evaluation of the temperature profiles in the time intervals in which the pyrometer starts the measurement ahead of the pool (when IT is reached) and before the pyrometer beam leaves the layer (intervals delimited by the vertical dashed red lines in Figs. 5 and 6). To better visualise this behaviour, the temperature value recorded just before the exit of the measurement point is positioned right next to the vertical dashed red lines. They are presented for each interlayer temperature level, except for the 100 °C, which showed practically no variation. It is possible to note in Figs. 5 and 6 that the temperature deviation from the set IT to that measured at the moment before the exit of the measurement point is slightly smaller as more layers are deposited. Despite interlayer temperature control, this behaviour is likely from a heat accumulation that occurs along the layer depositions. The steady state can eventually be reached with a constant temperature deviation.

Table 2 shows the same data from another perspective, i.e., the temperature variability along the layer length ($\Delta T/\Delta LL$), quantified in °C/mm, which represents the variability of the monitored temperature in relation to IT along the layer length (usable ΔLL of 120 mm, when the pyrometer was measuring). One can verify in Table 2 that $\Delta T/\Delta LL$ tends to turn significantly higher as IT increases. $\Delta T/\Delta LL$ decreases slightly with the building direction (Z), that is, when more layers are deposited. The wire feed speed with travel speed combination also affects the $\Delta T/\Delta LL$ (in this case, slower WFS and TS delivered more temperature variability along the layer length). These findings show the presence of a thermal gradient established throughout the wall during the deposition of a layer monitored by the pyrometer ahead of the arc, a common approach for closed-loop control in WAAM. The influence of this gradient on the wall dimension (widths and heights) has not been thoroughly studied,

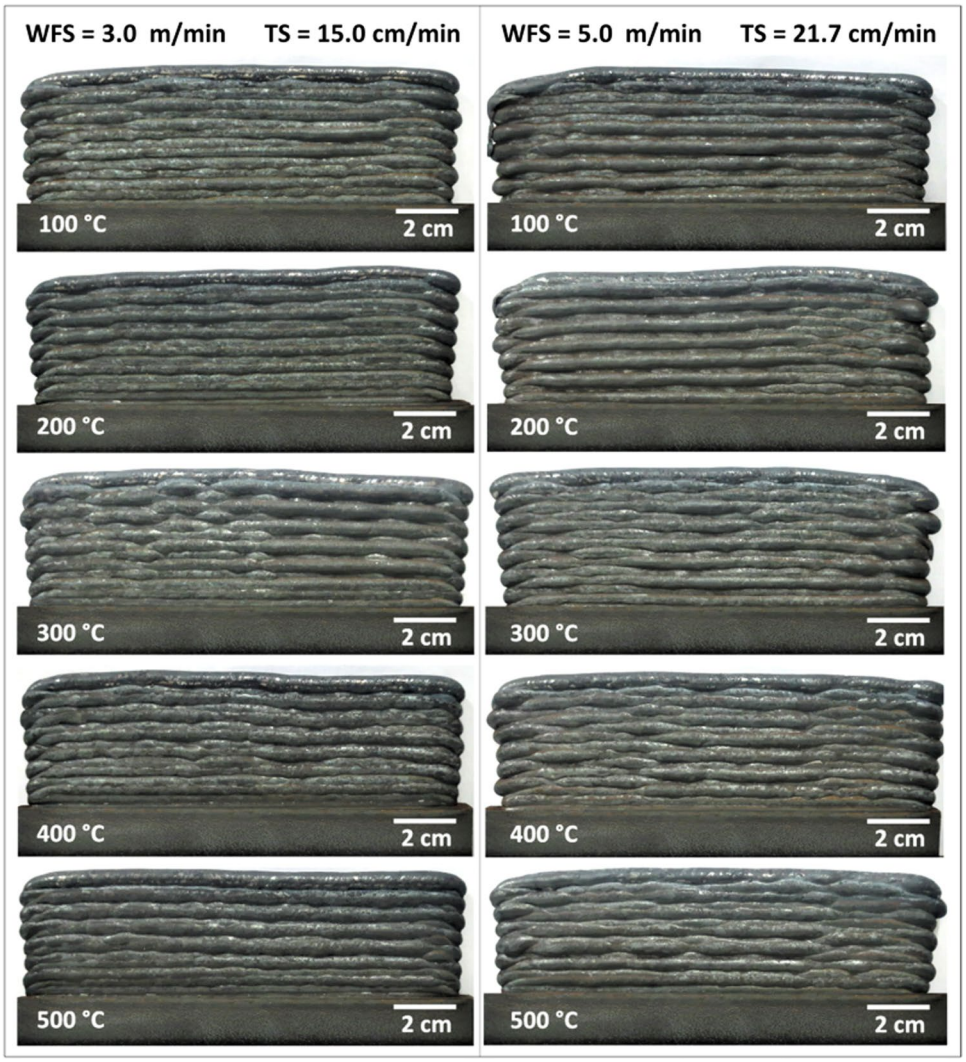

Fig. 4 Wall surface aspect from the preliminary tests (experimental matrix in Table 1)

but Jorge et al. [13] have shown that one should not expect dimensional changes, since the temperature under the pool (more influential on the layer shape) is almost constant.

Back to the scope of the work, Fig. 7 presents the geometrical features from the preliminary tests. In general, for the same WFS with TS combination, increasing IT implies greater external (WW_{ext}) and effective (WW_{eff}) wall widths and lower layer heights (LH). In terms of welding processes, it is already known that the higher the interpass temperature, the wider and shorter the bead, due to the increase in wettability, promoted by higher temperature in the bead vicinity. In the case of thin walls deposited by additive manufacturing itself, it is possible that wettability also has a degree of contribution. However, this phenomenological contribution should be lesser, since the width of the previous layer becomes a limiting factor. Thus, the viscosity of the molten pool can be pointed out as another factor to explain the observed effect. In this case, increasing interlayer temperature should decrease the cooling rate, making the viscosity lower for longer. This makes the pool less resistant to the movement induced by arc pressure, resulting in a wider (wall width) and shorter (layer height) geometry.

Examining Fig. 7c in particular, and considering the same WFS with TS combination, it can be seen that the surface waviness (SW) is a geometrical feature less sensitive to change in interlayer temperature. When evaluating the same IT and contrasting the two combinations of wire feed speed with travel speed, it is possible to verify that the sizes of WW_{ext}, SW, and LH tended to be, in general, slightly higher for the combination of WFS at 5.0 m/min and TS at 21.7 cm/min. At the same time, the WW_{eff} values were relatively close to each other (except for the results obtained for IT of 500 °C). The difference in the amount of material deposited per unit length may account for this effect. The combination of WFS at 3.0 m/min and TS at 15.0 cm/min deposited 0.17 kg/m on average, while the combination of WFS at 5.0 m/min and TS at 21.7 cm/min deposited 0.20 kg/m on average.

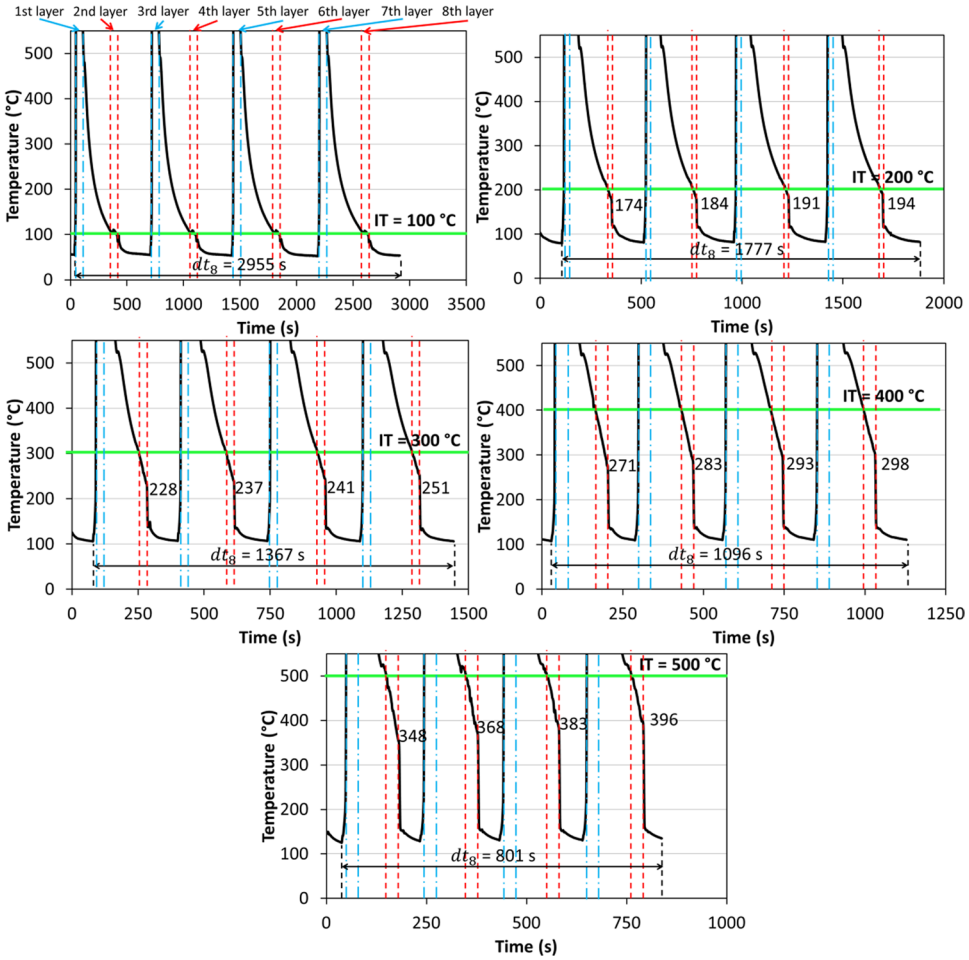

Fig. 5 Temperature traces at the different interlayer temperatures (IT), using WFS at 3.0 m/min and TS at 15.0 cm/min, where dt_8 represents the sum of deposition and idle times after the deposition of the eight layers — the horizontal continuous green lines indicate the reference level of IT for starting a new layer, while the vertical dashed red lines are the time intervals in which the pyrometer measures the temperature ahead of the molten pool (between lines 4 and 5 of Fig. 2b) and the vertical dashed-dot blue lines are the time intervals in which the pyrometer measures the temperature behind the molten pool (between lines 2 and 3 of Fig. 2b)

3.2 Main tests

The main tests aimed at evaluating the combined effect of the interlayer temperature (IT) with travel speed (TS) for a given wire feed speed (WFS) on the WAAM performance (operational, geometrical and metallurgical) of thin walls with the same target effective wall width (WW_{eff}) (arbitrarily chosen as 5.7 mm). The choice of parameters for the main tests was based on two basic premises: (a) the fastest WFS as feasible; (b) the wider IT range. A WFS of 5.0 m/min (the higher WFS level employed in the preliminary tests) and three interlayer temperature levels (100, 300, and 500 °C) composed the DoE, using not only natural cooling (NC) but also near immersion active cooling (NIAC), as justified in the methodology (first part of Section 2). As seen in the preliminary tests (Section 3.1), IT influences the WW_{eff} dimension (Fig. 7b). Consequently, a faster travel speed value had to be determined for each IT level above 100 °C to make up for this influence. However, the authors did not have data that could be used to correlate TS to wall width for different IT values. Prior experiments were conducted to determine the TS needed to reach a target WW_{eff} with WFS at 5.0 m/min to overcome this setback. Then, six walls were deposited in total during the main tests, three with NC and another three using NIAC, according to the DoE of Table 3.

Table 4 presents the set and monitored parameters from the experimental conditions in Table 3. The combined IT and TS variations for the same WFS do not affect either current (I_m or I_{rms}) or voltage (V_m or V_{rms}), supporting the test robustness. Naturally, the mean arc energy (E_m) decreases with faster TS.

Figure 8 shows the surface aspect obtained for each wall. For the same cooling approach, it is possible to see that lower interlayer temperature (consequently, also slower TS to reach the same WW_{eff}) led to a worse superficial aspect, which agrees with Geng et al. [10] and Knezovic et al. [16]. In the attempt to explain the surface aspect, on the one hand, lower IT would tend to promote more rigid pools, since higher cooling rates should potentially guarantee lower volume and higher viscosity to the molten pool. Therefore, a molten pool with higher resistance to the movement induced by arc pressure. On the other hand, the higher amount of material deposited per unit of length, which is achieved with lower travel speed at the same wire feed speed, increases

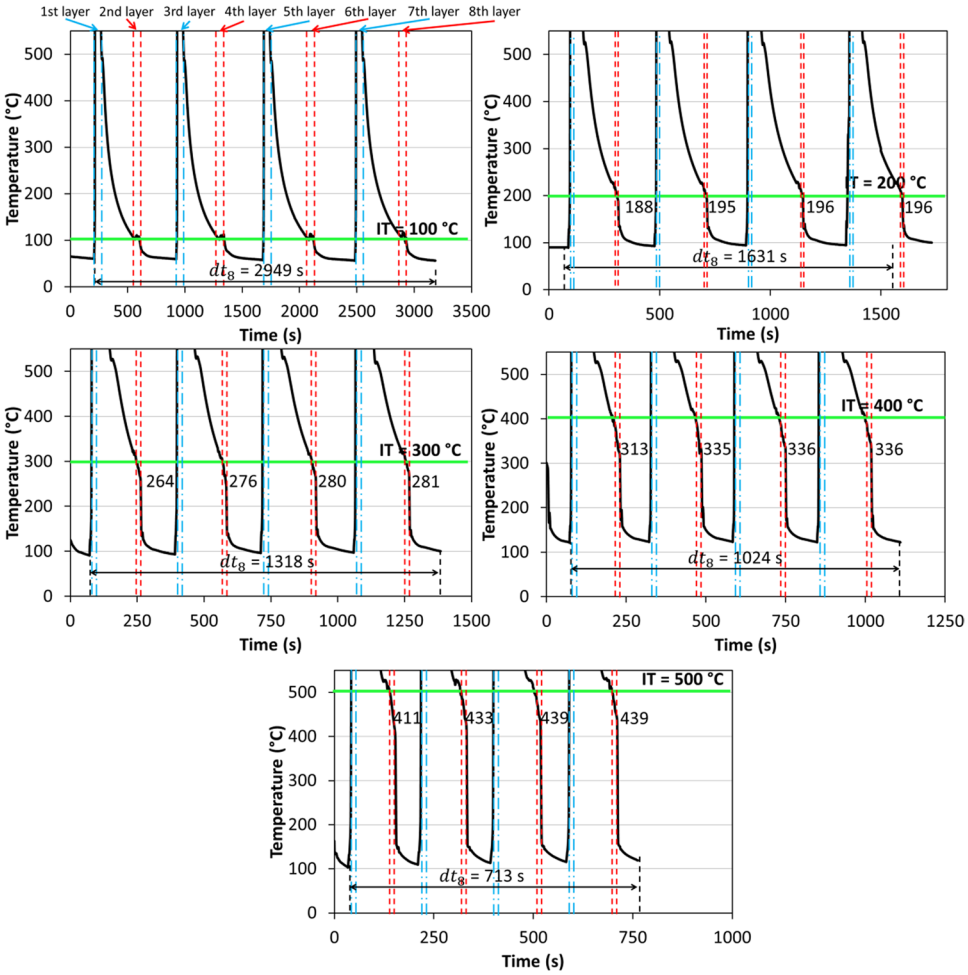

Fig. 6 Temperature traces at the different interlayer temperatures (IT), using WFS at 5.0 m/min and TS at 21.7 cm/min, where dt_8 represents the sum of deposition and idle times after the deposition of the eight layers — the horizontal continuous green lines indicate the reference level of IT for starting a new layer, while the vertical dashed red lines are the time intervals in which the pyrometer measures the temperature ahead of the molten pool (between lines 4 and 5 of Fig. 2b) and the vertical dashed-dot blue lines are the time intervals in which the pyrometer measures the temperature behind the molten pool (between lines 1 and 3 of Fig. 2b)

Table 2 Temperature variability along the layer length (ΔT/ΔLL), quantified in °C/mm, of the walls built according to the experimental matrix in Table 1

IT (°C)	WFS = 3 m/min; TS = 15 cm/min				WFS = 5 m/min; TS = 21.7 cm/min			
	2nd layer	4th layer	6th layer	8th layer	2nd layer	4th layer	6th layer	8th layer
100	0.0	0.0	0.0	0.0	0.0	0.0	0.0	0.0
200	0.2	0.1	0.1	0.1	0.1	0.0	0.0	0.0
300	0.7	0.6	0.5	0.4	0.3	0.2	0.2	0.2
400	1.2	1.1	1.0	0.9	0.8	0.6	0.6	0.6
500	1.4	1.2	1.1	0.9	0.8	0.6	0.6	0.6

the volume of the molten pool and tends to a more unstable pool (more susceptible to bead irregularities for the same arc pressure). Based on the observed behaviour, the effect promoted by the higher amount of material deposited appears predominant. Taking now the same parameter combinations, no significant change is observed in the surface aspect when comparing the two cooling approaches, corroborating the detrimental effect of a higher amount of material deposited per unit of length in relation to faster cooling.

Figure 9 presents the temperature profiles corresponding to the layer-related cycles of torch movement, similar to Figs. 5 and 6. Under the same cooling approach (natural cooling (NC) — or near immersion active cooling (NIAC)), lower IT-TS combinations led to longer production times (dt_8), since this parameter combination govern cooling time between layers. When comparing the two cooling approaches for the same IT-TS combination, the NIAC conditions presented a considerably lower dt_8, due to the higher cooling rate exerted by the heat exchange between the wall and the water. It is also confirmed in Fig. 9 that the trend discussed during the preliminary tests was maintained, that is, the temperature deviation from the set interlayer temperature to that measured at the moment before the exit of the measurement point is slightly smaller as more layers are

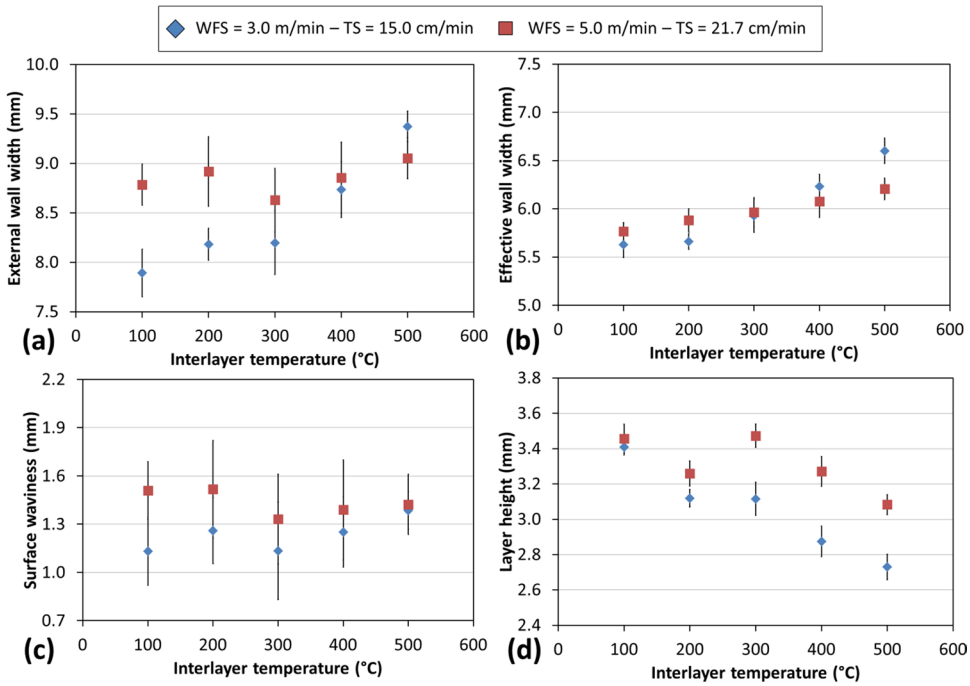

Fig. 7 Geometrical features from the preliminary experiments (according to Table 1): **a** external wall width; **b** effective wall width; **c** surface waviness; and **d** layer height (where: WFS, wire feed speed and TS, travel speed)

Table 3 Experimental matrix for the main tests (target effective wall width of 5.7 mm and wire feed speed of 5 m/min)

Cooling approach	IT (°C)	TS (cm/min)
Natural cooling (NC)	100	21.7
Natural cooling (NC)	300	28.4
Natural cooling (NC)	500	33.3
Near immersion active cooling (NIAC)	100	21.7
Near immersion active cooling (NIAC)	300	28.4
Near immersion active cooling (NIAC)	500	33.3

deposited (due to heat accumulation). In the condition with IT at 300 °C and TS at 28.4 cm/min (Fig. 9d), for example, a temperature variation of almost 200 °C was achieved along the layer. Compared with IT at 500 °C and TS at 33.3 cm/min (Fig. 9f), a significant difference, greater than 300 °C, was recorded. These results reinforce the recommendation to have monitored the magnitude of the thermal gradient along the layer.

Table 5 shows the temperature variability along the layer length (ΔT/ΔLL). One can verify that ΔT/ΔLL tends to turn significantly higher as IT with TS combination increases, mainly under NIAC (even for IT = 100 °C), due to the more intense thermal gradient generated between layers. However, ΔT/ΔLL does not vary significantly in the building (Z) direction, when more layers are deposited under the same interlayer temperature and cooling approach.

Figure 10 presents the macrographic view of the walls built during the main tests. As seen, the profiles are affected by IT-TS combinations, yet no imperfections are noticed. Figure 11 presents the geometrical features of the walls built during the main tests. From Fig. 11a, it is possible to verify that the effective average wall widths (WW_{eff}) were equal to each other and matched the target value for the different IT with TS combinations using the natural cooling (NC)

Table 4 Monitored (averages from 10 layers) mean wire feed speed (WFS_m), mean and RMS current (I_m and I_{rms}), mean and RMS voltage (V_m and V_{rms}), and mean arc energy per unit length (E_m), according to the experimental matrix in Table 3 (where: NC, natural cooling; NIAC, near immersion active cooling; IT, interlayer temperature; and TS, travel speed)

Cooling	IT (°C)	TS (cm/min)	WFS_m (m/min)	I_m (A)	I_{rms} (A)	V_m (V)	V_{rms} (V)	E_m (J/mm)
NC	100	21.7	5.1 ± 0.1	162.1 ± 0.6	181.9 ± 0.5	13.2 ± 0.1	16.5 ± 0.1	702.2 ± 6.9
NC	300	28.4	5.1 ± 0.3	160.9 ± 1.1	181.2 ± 0.9	13.4 ± 0.2	16.8 ± 0.2	558.3 ± 8.9
NC	500	33.3	5.1 ± 0.2	162.7 ± 0.4	182.4 ± 0.4	13.4 ± 0.2	16.8 ± 0.2	473.6 ± 6.8
NIAC	100	21.7	5.1 ± 0.2	161.7 ± 0.4	181.7 ± 0.4	13.3 ± 0.1	16.6 ± 0.1	711.9 ± 8.3
NIAC	300	28.4	5.2 ± 0.2	161.4 ± 0.8	181.3 ± 0.7	13.4 ± 0.3	16.8 ± 0.2	549.7 ± 9.3
NIAC	500	33.3	5.2 ± 0.2	161.5 ± 0.8	181.5 ± 0.8	13.4 ± 0.2	16.9 ± 0.2	457.6 ± 5.3

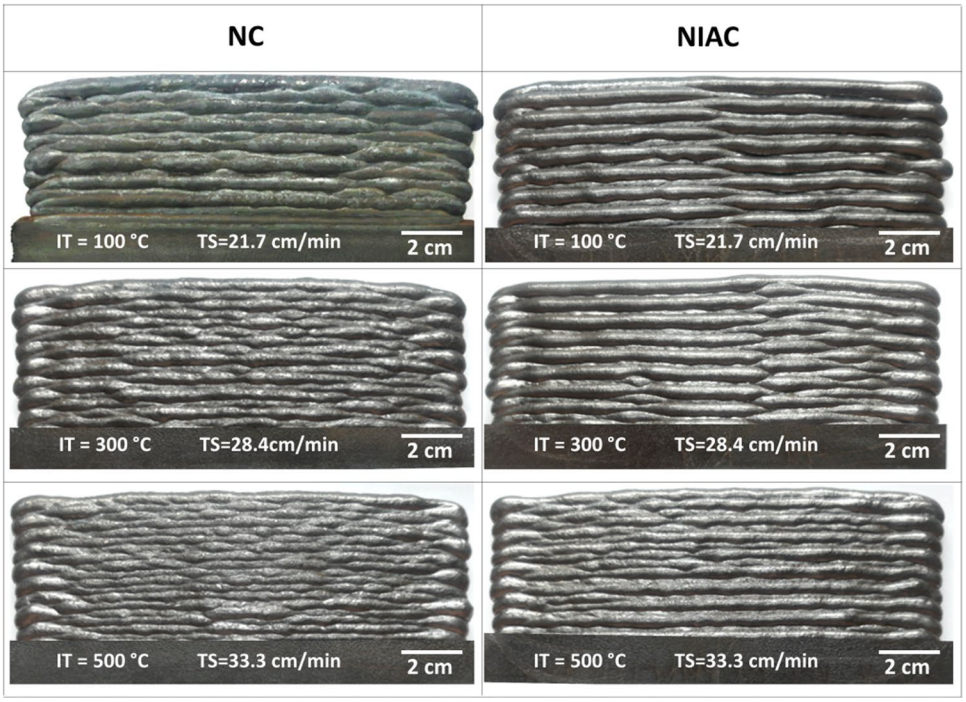

Fig. 8 Wall surface aspect from the main tests (experimental matrix in Table 3)

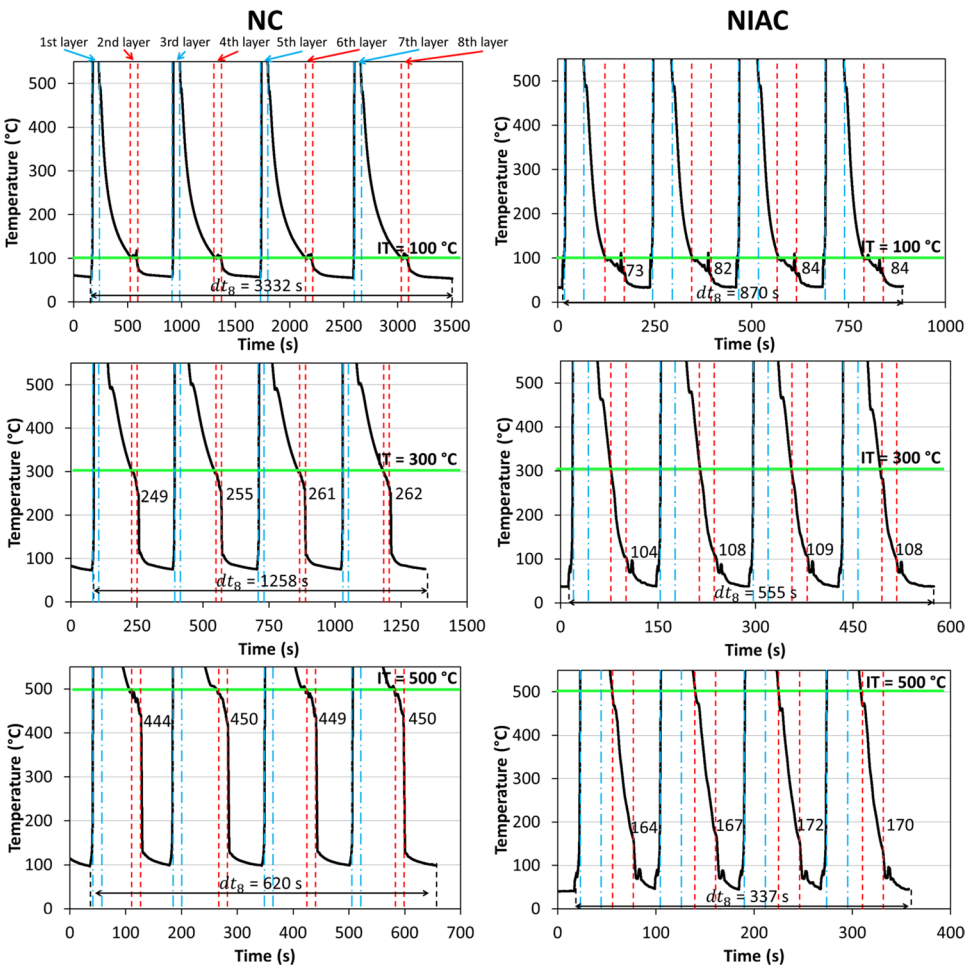

Fig. 9 Temperature traces at the different interlayer temperatures (IT) from the experimental matrix in Table 3, where dt_8 represents the sum of deposition and idle times after the deposit of the eight layers — the horizontal continuous green lines indicate the reference level of IT for starting a new layer, while the vertical dashed red lines are the time intervals in which the pyrometer measures the temperature ahead of the molten pool during layer deposition (between lines 4 and 5 of Fig. 2b) and the vertical dashed-dot blue lines are the time intervals in which the pyrometer measures the temperature behind the molten pool (between lines 2 and 3 of Fig. 2b)

Table 5 Temperature variability along the layer length (ΔT/ΔLL), quantified in °C/mm, of the walls built according to the experimental matrix in Table 3

Factors			ΔT/ΔLL (°C/mm)			
Cooling	IT (°C)	TS (cm/min)	2nd layer	4th layer	6th layer	8th layer
NC	100	21.7	0.0	0.0	0.0	0.0
NC	300	28.4	0.5	0.4	0.4	0.3
NC	500	33.3	0.5	0.5	0.5	0.5
NIAC	100	21.7	0.2	0.2	0.1	0.1
NIAC	300	28.4	1.8	1.7	1.7	1.7
NIAC	500	33.3	3.1	3.0	3.0	3.0

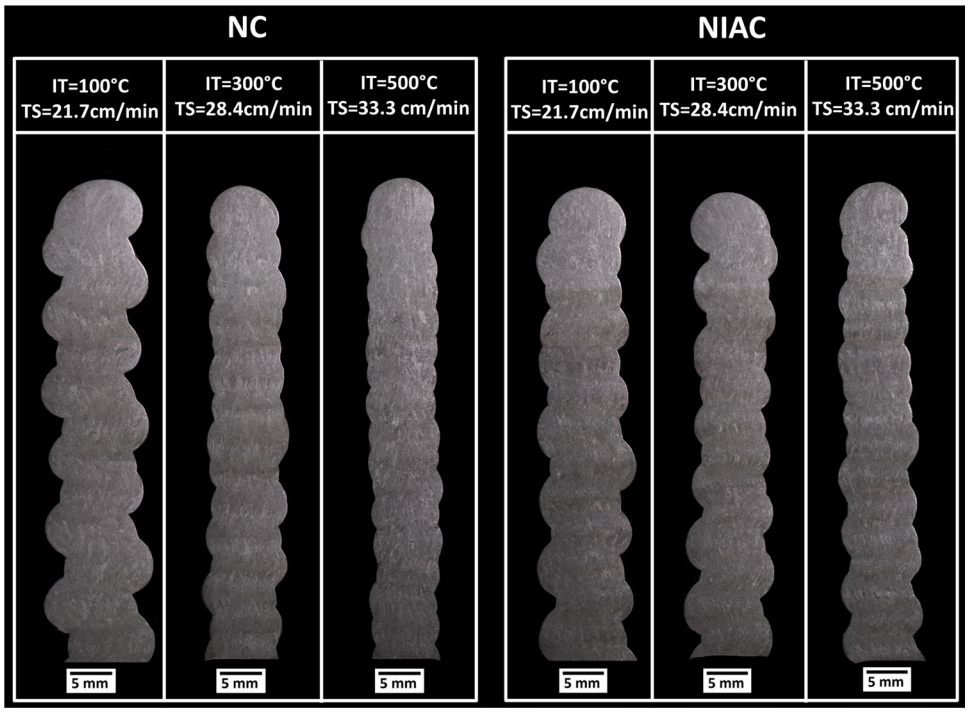

Fig. 10 Cross-section macrographs of the walls from the main tests

approach. It is worth remembering that all the considerations taken to select TS levels for each pre-established IT level (100, 300, and 500 °C), in an attempt to achieve a WW_{eff} of 5.7 mm, were based on walls deposited under NC. Then, the outcomes justify the agreement of these results for this cooling approach and attest to the consistency of the experimental work. With the conditions under near immersion active cooling (NIAC), in turn, at first view, WW_{eff} and WW_{ext} averages tended to not match with the walls cooled under NC and decrease as the combined IT with TS increased (Fig. 11a and b). This NIAC-driven trend is not expected, because heat extraction with this approach acts only at a given distance from the pool (a layer-edge to water distance of 20 mm) and WFS is the same for each IT with TS combination. Indeed, in another piece of work [31], in which NIAC and NC approaches were compared to WAAM build of thin walls with an aluminium alloy (ER 5356), both cooling methods led to quite similar geometries if equivalent interlayer temperatures were applied (the total deposition time with the natural cooling approach is also significantly extended due to the need for a long idle time between layers).

As Fig. 11a left the authors in doubt about the effect of the NIAC approach on the wall width, four cross-sections were taken from each 3D mesh of the walls (Fig. 12). Their areas were quantified to assess whether the amount of material deposited per unit of length was actually maintained for the same parameter combination. As seen, the cross-section areas were practically the same indifferent to the cooling approaches with the same parameter combination. This means that the same amount of material per unit of length was deposited.

Then, the justification for the unexpected variation of the wall widths when compared to walls built under NC and NIAC (Fig. 11a and b) can be based on some reasonings. First, one would expect a layer height (LH) increase as wall width decreases and vice-versa, since the amount of material per unit of length is the same for each IT with TS combination (Fig. 12). But LH did not decrease with NIAC

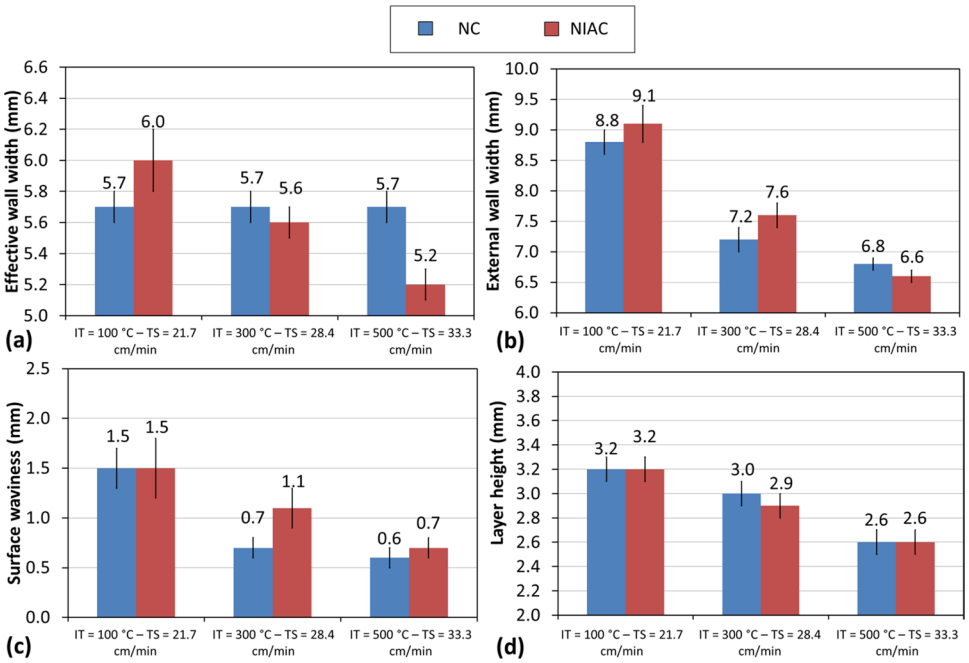

Fig. 11 Geometrical features from the main experiments (according to Table 4): **a** effective width wall (WW_{eff}); **b** external wall width (WW_{ext}); **c** surface waviness (SW); and **d** layer height (LH) (where: NC, natural cooling; NIAC, near immersion active cooling; IT, interlayer temperature; and TS, travel speed)

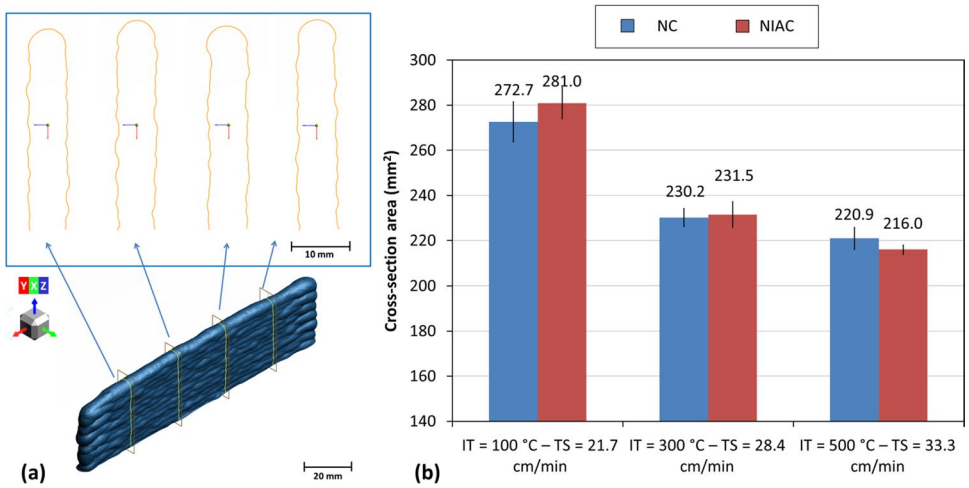

Fig. 12 3D scanned features from the main experiments (according to Table 3): **a** profiles of the cross-section areas; and **b** cross-section areas (where: NC, natural cooling; NIAC, near immersion active cooling; IT, interlayer temperature; and TS, travel speed)

(Fig. 11d); on the contrary, they matched those with NC. Second, only slightly higher width values (both effective and external) were observed with NIAC conditions when IT-TS was the lowest. And the inverse occurred as IT-TS was assumed to have the highest value, i.e., not keeping the same trend (random behaviour). Third, the difference in wall widths between NC and NIAC is short, 0.3 mm on average. LH was determined using a 0.05-mm-resolution calliper, while the WW_{eff} and WW_{ext} averages were taken using a 3D scanner (see Section 2.2). The potentially higher uncertainties from the 3D scanner measurement could justify the variation.

Concerning metallurgical features, no marked microstructural differences were observed between the different experimental conditions evaluated and illustrated in Figs. 13 and 14. A microstructure composed mainly of martensite and bainite is evidenced, regardless of the position along the building direction (Z). One must remember that higher interlayer temperature values were combined with faster travel speed levels (consequently, arc energy decreased) to maintain the same target WW_{eff}. On the one hand, this means that cooling rates must be slowed down by using a higher IT. On the other hand, cooling rates become faster due to higher TS (lower arc energy). Considering the predominant heat transfer mechanism (conduction), the cross-sectional area is another factor that also governs the heat flux through the wall. Figure 12 shows that the cross-sections are statistically equal between the two cooling approaches for the same combination of parameters. Still, a parallel increase in IT and TS led to smaller cross sections, resulting in a

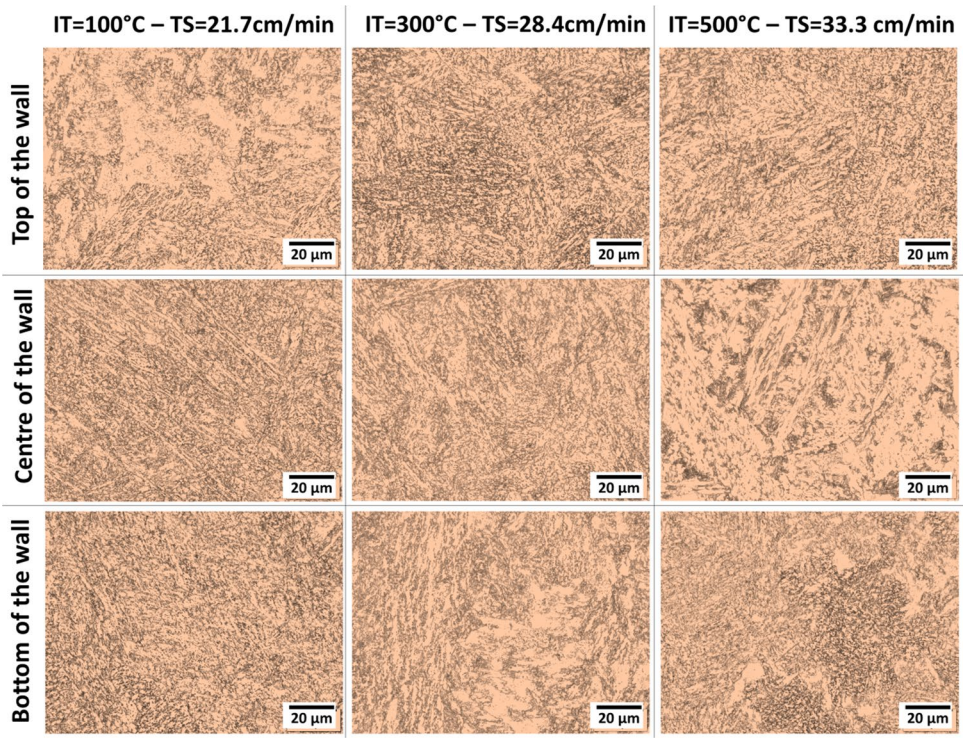

Fig. 13 Representative OM micrographs from the top layer, and from the centre and bottom of the walls deposited with the experimental conditions of Table 3, using natural cooling (where: IT, interlayer temperature and TS, travel speed)

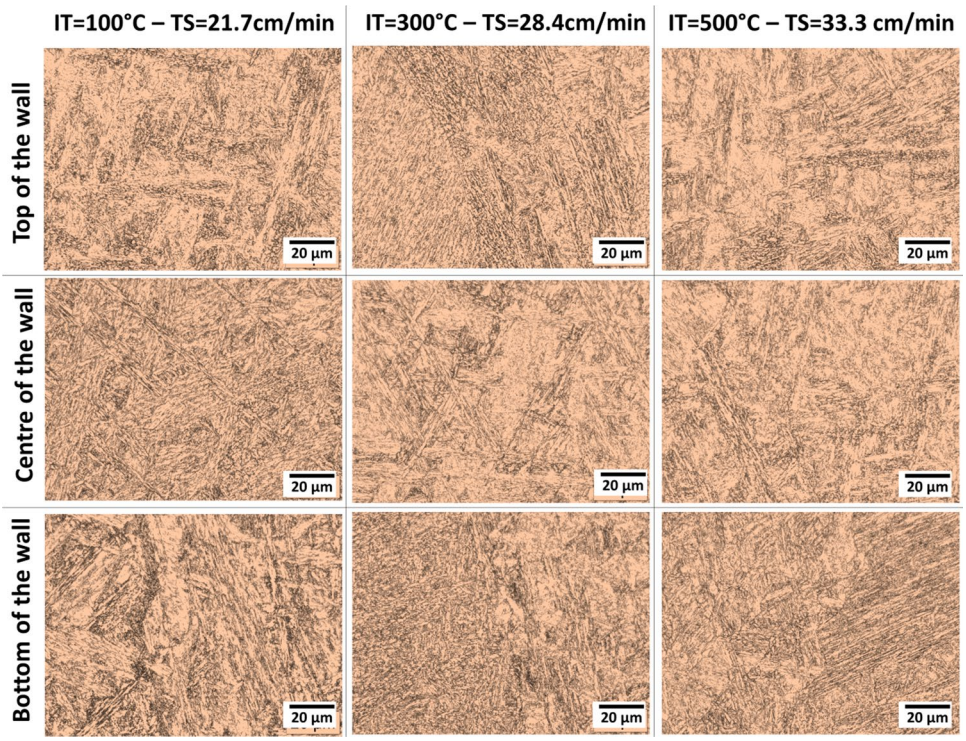

Fig. 14 Representative OM micrographs from the top layer, and from the centre and bottom of the walls with the experimental conditions in Table 3, using near immersion active cooling (where: IT, interlayer temperature and TS, travel speed)

lower conduction heat flux (slower cooling rates). Despite the existence of all these factors that govern the cooling rate, it is still possible that the cooling rates of the evaluated parameter combinations are maintained in the same region (in relation to the transformation curves) of the continuous cooling transformation diagram, leading to the observed microstructural similarity.

Figure 15 shows each experimental condition's microhardness profiles (a downward profile with approximately 15 indentations). In general, less dispersed (lower standard

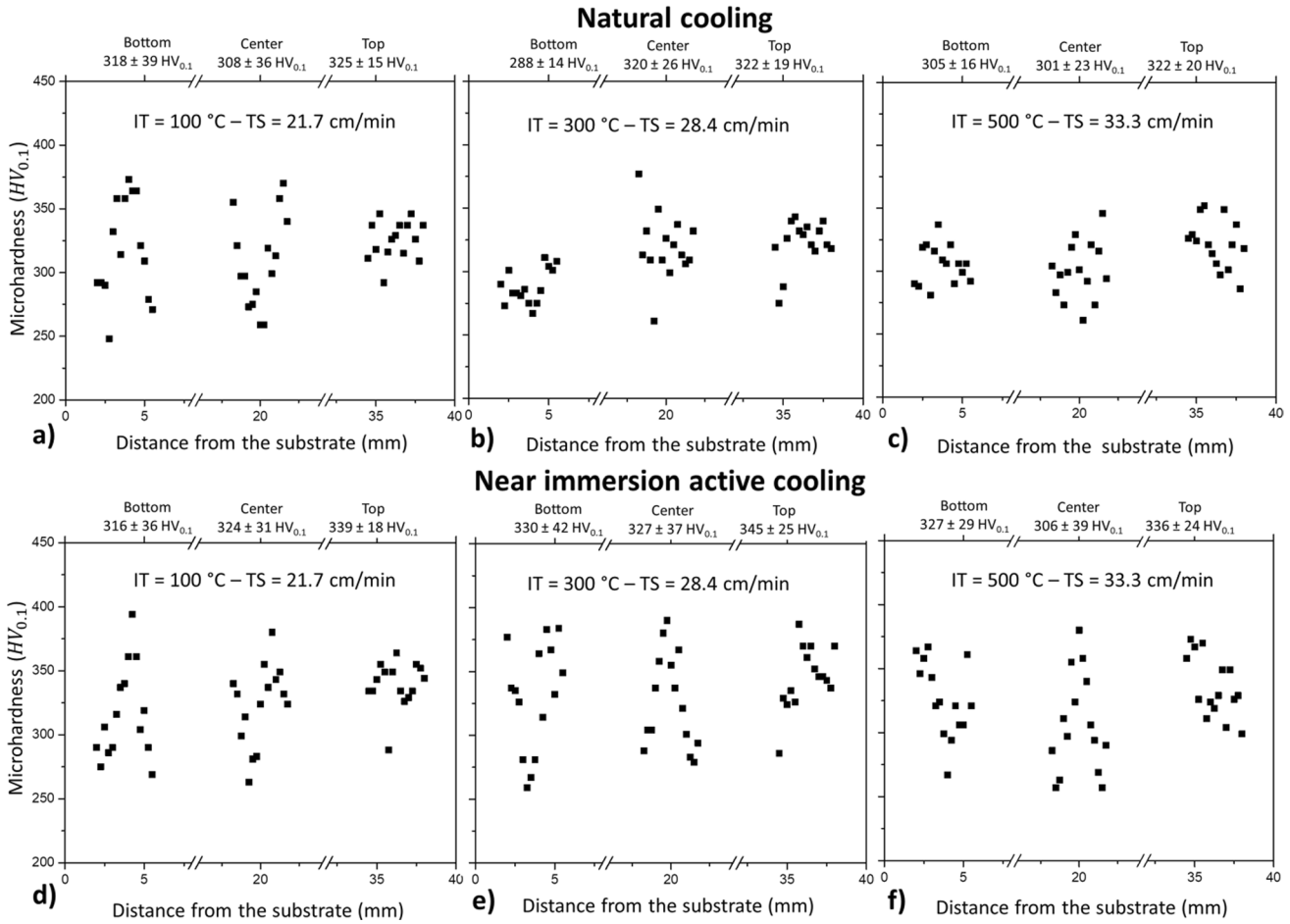

Fig. 15 Microhardness profile with different combinations of interlayer temperatures (IT) and travel speeds (TS), with natural cooling (upper) and near immersion active cooling (lower)

deviations) indentations are observed at the top layer regions of the walls, resembling a cluster. These regions (last and penultimate layers) sustain mainly primary solidification structure, not experiencing reheating (predominantly non-tempered martensite). However, the centre and bottom of the wall represent better a WAAM multiple-layer-single track build. Therefore, the microhardness analysis will concentrate on these wall areas. In most cases of the bottom and centre regions, microhardness ranged from 250 to 400 HV, following a V-profile (suggesting bands of harder and softer microconstituents). The harder values could represent coarse recrystallised martensite, while the softer values could mean tempered martensite due to the incidence of multiple thermal cycles. When the cooling approach between layers was natural (NC), the hardness dispersion got narrower and with less incidence of indentations as hard as 400 HV when IT (and TS) increased. However, this behaviour did not occur under near immersion active cooling, which imposes a faster cooling rate under the layers (surpassing the IT-TS effect on cooling rates). Natural cooling, mainly at higher interlayer temperature, may have provided longer times within the temperature range for tempering, resulting in microhardness being less dispersed and concentrated at lower values.

4 Conclusions

The global objective of this work was to assess the combined effect of the interlayer temperature (IT) with travel speed (TS) for a given wire feed speed (WFS) on operational (surface aspect, production time and temperature profile), geometrical (wall width and height), and metallurgical (microstructure and microhardness) features of thin walls with the same width deposited by WAAM, using or not active cooling. An IT range definition that could be used in experimental design and heat distribution on the wall were the specific objectives. A low carbon-low alloy steel (2.5Cr-1Mo) wire, shielded with a $96\%Ar + 4\%CO_2$ blend, was used with the GMAW CMT for the depositions.

1. From the results linked to the specific objective, it was possible to conclude that:

- IT between 100 and 500 °C is suitable to operate with this material and within the range of WFS and TS chosen for this work, since no molten pool collapse occurs;
- For the same WFS with TS combination, the higher the IT, the greater the temperature variability along the layer length (ΔT/ΔLL), quantified in °C/mm, considering a pyrometric measurement point ahead of the arc at 30 mm;
- Assuming the same IT, higher WFS with TS combination led to lower ΔT/ΔLL;
- In general, as long as the same WFS with TS combination is considered, the increase in IT implied greater external and effective wall widths (WW_{ext} and WW_{eff}, respectively), and lower layer heights (LH).

2. From the results linked to the global objective (which is restrained to a same effective wall width (WW_{eff}) and the set WFS), it was possible to conclude that:

- A smoother surface appearance (waviness) with the same effective wall width is obtained with higher IT with TS combination, regardless of the cooling approach (either natural cooling (NC) or near immersion active cooling (NIAC));
- If the same deposition parameters (IT-TS) combination is employed, a shorter production time is achieved on walls under NIAC than NC.
- Concerning the temperature profile, a more significant temperature variability along the layer length (ΔT/ΔLL) is observed increasing IT-TS combination and under NIAC, with IT measured 30 mm ahead of the arc;
- The cooling approaches (NC or NIAC) do not affect either the wall width (effective or external) or the layer height. However, they are affected by the IT with TS combination (the higher the IT-TS combination, the thinner and shorter the width and height, respectively).
- No remarkable microstructural differences were observed as a function of IT combined to TS (for such low alloy steel), either when NC or NIAC was used, although there was a variation of arc energy (proportional to TS) and IT. However, some tempering (microhardness reduction) was observed in the walls deposited under NC, using higher IT (300 e 500 °C).

It is important to note that the findings linked to the global objective are tied up to a specific WFS level (5 m/min). Thus, a parameterisation with another WFS value (different current level as well) will need different IT-TS combinations to achieve the same effective width. This, of course, can lead to other operational, geometric, and metallurgical values. However, despite not being studied in this work, the trends will probably be the same as the IT-TS combinations change.

Acknowledgements The authors would like to thank the Center for Research and Development of Welding Processes of the Federal University of Uberlandia (Laprosolda-UFU) for the laboratory infrastructure and technical support.

Author contribution State-of-the-art survey: Felipe Ribeiro Teixeira and Américo Scotti. Conceptualization and methodology: Felipe Ribeiro Teixeira, Fernando Matos Scotti, Vinicius Lemes Jorge, and Américo Scotti. Experimental development: Felipe Ribeiro Teixeira, Fernando Matos Scotti, and Vinicius Lemes Jorge. Analyses of results and manuscript writing: Felipe Ribeiro Teixeira, Fernando Matos Scotti, Vinicius Lemes Jorge, and Américo Scotti.

Funding Open access funding provided by University West. This work was supported by The National Council for Scientific and Technological Development – CNPq (grant numbers 302863/2016–8), The Coordination for the Improvement of Higher Education Personnel – CAPES (Finance Code 001), and PETROBRAS (project number 23117.018175/2019–80).

Availability of data and material The datasets used or analysed during this research are available from the corresponding author on reasonable request.

Declarations

Ethical approval The manuscript is all original, i.e., none of these parts has been published before, and it is not has been submitted for publication anywhere else.

Consent to participate Consent to participate was obtained from all individual participants included in the study.

Consent for publication Consent to publish was obtained from all individual participants included in the study.

Competing interests The authors declare no competing interests.

References

1. Zuo X, Zhang W, Chen Y, Oliveira JP, Zeng Z, Li Y, Luo Z, Ao S (2022) Wire-based directed energy deposition of NiTiTa shape memory alloys: microstructure, phase transformation, electrochemistry,

X-ray visibility and mechanical properties. Addit Manuf 59: 103115. https://doi.org/10.1016/j.addma.2022.103115
2. Rodrigues TA, Duarte VR, Miranda RM, Santos TG, Oliveira JP (2021) Ultracold-wire and arc additive manufacturing (UC-WAAM). J Mater Process Technol 296: 117196. https://doi.org/10.1016/j.jmatprotec.2021.117196
3. Müller J, Grabowski M, Müller C, Hensel J, Unglaub J, Thiele K, Kloft H, Dilger K (2019) Design and parameter identification of wire and arc additively manufactured (WAAM) steel bars for use in construction. Metals 9(7):725. https://doi.org/10.3390/met9070725
4. Müller C, Müller J, Kloft H, Hensel J (2022) Design of structural steel components according to manufacturing possibilities of the robot-guided DED-arc process. Buildings 12(12):2154. https://doi.org/10.3390/buildings12122154
5. Da Silva LJ, Reis RP, Scotti A (2019) The potential of IR pyrometry for monitoring interpass temperature in wire + arc additive manufacturing. Evol Mech Eng 3 (1). https://doi.org/10.31031/eme.2019.03.000553
6. Chen W, Chen Y, Zhang T, Wen T, Yin Z, Feng X (2020) Effect of ultrasonic vibration and interpass temperature on microstructure and mechanical properties of Cu-8Al-2Ni-2Fe-2Mn alloy fabricated by wire arc additive manufacturing. Metals 10(2):215. https://doi.org/10.3390/met10020215
7. Derekar K, Lawrence J, Melton G, Addison A, Zhang X, Xu L (2018) Influence of interpass temperature on wire arc additive manufacturing (WAAM) of aluminium alloy components. MATEC Web Conf - International Conference on Advanced Welding and Smart Fabrication Technologies 269:5001. https://doi.org/10.1051/matecconf/201926905001
8. Nemani AV, Ghaffari M, Salahi S, Lunde J, Nasiri A (2021) Effect of interpass temperature on the formation of retained austenite in a wire arc additive manufactured ER420 martensitic stainless steel. Mater Chem Phys 266 (1): 124555. https://doi.org/10.1016/j.matchemphys.2021.124555
9. Shen C, Pan Z, Cuiuri D, Ding D, Li H (2017) Influences of deposition current and interpass temperature to the Fe3Al-based iron aluminide fabricated using wire-arc additive manufacturing process. Int J Adv Manuf Technol 88:2009–2018. https://doi.org/10.1007/s00170-016-8935-3
10. Geng H, Li J, Xiong J, Lin X (2016) Optimisation of interpass temperature and heat input for wire and arc additive manufacturing 5A06 aluminium alloy. Sci Technol Weld Join 22(6):472–483. https://doi.org/10.1080/13621718.2016.1259031
11. Montevecchi F, Venturini G, Grossi N, Scippa A, Campatelli G (2018) Idle time selection for wire-arc additive manufacturing: a finite element-based technique. Addit Manuf 21:479–486. https://doi.org/10.1016/j.addma.2018.01.007
12. Müller J, Hensel J, Dilger K (2021) Mechanical properties of wire and arc additively manufactured high-strength steel structures. Weld World 66:395–407. https://doi.org/10.1007/s40194-021-01204-1
13. Jorge VL, Teixeira FR, Scotti A (2022) Pyrometrical interlayer temperature measurement in WAAM of thin wall: strategies, limitations and functionality. Metals 12(5):765. https://doi.org/10.3390/met12050765
14. Wu B, Ding D, Pan Z, Cuiuri D, Li H, Han J, Fei Z (2017) Effects of heat accumulation on the arc characteristics and metal transfer behavior in wire arc additive manufacturing of Ti6Al4V. J Mater Process Technol 250:304–312. https://doi.org/10.1016/j.jmatprotec.2017.07.037
15. Wang Z, Zimmer-Chevret S, Léonard F, Abba G (2021) Prediction of bead geometry with consideration of interlayer temperature effect for CMT-based wire-arc additive manufacturing. Weld World 65:2255–2266. https://doi.org/10.1007/s40194-021-01192-2
16. Knezović N, Garašić I, Jurić I (2020) Influence of the interlayer temperature on structure and properties of wire and arc additive manufactured duplex stainless steel product. Mater 13(24):5795. https://doi.org/10.3390/ma13245795
17. Spencer JD, Dickens PM, Wykes CM (1998) Rapid prototyping of metal parts by three-dimensional welding. Proc Inst Mech Eng Part B J Eng Manuf 212(3):175–182. https://doi.org/10.1243/0954405981515590
18. Ali Y, Henckell P, Hildebrand J, Reimann J, Bergmann JP, Barnikol-Oettler S (2019) Wire arc additive manufacturing of hot work tool steel with CMT process. J Mater Process Technol 269:109–116. https://doi.org/10.1016/j.jmatprotec.2019.01.034
19. Da Silva LJ, Souza DM, De Araújo DB, Reis RP, Scotti A (2020) Concept and validation of an active cooling technique to mitigate heat accumulation in WAAM. Int J Adv Manuf Technol 107:2513–2523. https://doi.org/10.1007/s00170-020-05201-4
20. Kozamernik N, Bračun D, Klobčar D (2020) WAAM system with interpass temperature control and forced cooling for near-net-shape printing of small metal components. Int J Adv Manuf Technol 110:1955–1968. https://doi.org/10.1007/s00170-020-05958-8
21. Hackenhaar W, Mazzaferro JAE, Montevecchi F, Campatelli G (2020) An experimental-numerical study of active cooling in wire arc additive manufacturing. J Manuf Process 52:58–65. https://doi.org/10.1016/j.jmapro.2020.01.051
22. Ma C, Li C, Yan Y, Liu Y, Wu X, Li D, Han Y, Jin H, Zhang F (2021) Investigation of the in-situ gas cooling of carbon steel during wire and arc additive manufacturing. J Manuf Process 67:461–477. https://doi.org/10.1016/j.jmapro.2021.05.022
23. Wu B, Pan Z, Ding D, Cuiuri D, Li H, Fei Z (2018) The effects of forced interpass cooling on the material properties of wire arc additively manufactured Ti6Al4V alloy. J Mater Process Technol 258:97–105. https://doi.org/10.1016/j.jmatprotec.2018.03.024
24. Scotti FM, Teixeira FR, Da Silva LJ, De Araújo DB, Reis RP, Scotti A (2020) Thermal management in WAAM through the CMT advanced process and an active cooling technique. J Manuf Process 57:23–35. https://doi.org/10.1016/j.jmapro.2020.06.007
25. Teixeira FR, Scotti FM, Reis RP, Scotti A (2021) Effect of the CMT advanced process combined with an active cooling technique on macro and microstructural aspects of aluminum WAAM. Rapid Prototyp J 27(6):1206–1219. https://doi.org/10.1108/RPJ-11-2020-0285
26. Rodrigues TA, Duarte V, Avila JA, Santos TG, Miranda RM, Oliveira JP (2019) Wire and arc additive manufacturing of HSLA steel: effect of thermal cycles on microstructure and mechanical properties. Addit Manuf 27:440–450. https://doi.org/10.1016/j.addma.2019.03.029
27. Laghi V, Palermo M, Gasparini G, Girelli VA, Trombetti T (2021) On the influence of the geometrical irregularities in the mechanical response of wire-and-arc additively manufactured planar elements. J Constr Steel Res178: 106490. https://doi.org/10.1016/j.jcsr.2020.106490
28. Martina F, Mehnen J, Williams SW, Colegrove P, Wang F (2012) Investigation of the benefits of plasma deposition for the additive layer manufacture of Ti–6Al–4V. J Mater Process Technol 212(6):1377–1386. https://doi.org/10.1016/j.jmatprotec.2012.02.002
29. Teixeira FR, Scotti FM, Vilarinho LO, Da Mota CAM, Scotti A (2021) Transferability of the working envelope approach for parameter selection and optimisation in thin wall WAAM. Int J Adv Manuf Technol 119:969–989. https://doi.org/10.1007/s00170-021-08326-2
30. Scotti FM (2021) Manufatura Aditiva por Deposição a Arco de Paredes Finas de Aço Inoxidável Super Duplex Com Resfriamento Ativo Por Quase-imersão. Dissertation (in portuguese), Federal University of Uberlandia. https://doi.org/10.14393/ufu.di.2021.471
31. Da Silva LJ, Ferraresi HN, Araújo DB, Reis RP, Scotti A (2021) Effect of thermal management approaches on geometry and productivity of thin-walled structures of ER 5356 built by wire + arc additive manufacturing. Coatings 11(9):1141. https://doi.org/10.3390/coatings11091141